Oh et al. *NPG Asia Materials* (2021) 13:10
https://doi.org/10.1038/s41427-021-00281-4

NPG Asia Materials

ARTICLE Open Access

Gate-tunable photodetector and ambipolar transistor implemented using a graphene/$MoSe_2$ barristor

Gwangtaek Oh[1], Ji Hoon Jeon[1], Young Chul Kim[2], Yeong Hwan Ahn[2] and Bae Ho Park[1]

Abstract
Next-generation electronic and optoelectronic devices require a high-quality channel layer. Graphene is a good candidate because of its high carrier mobility and unique ambipolar transport characteristics. However, the on/off ratio and photoresponsivity of graphene are typically low. Transition metal dichalcogenides (e.g., $MoSe_2$) are semiconductors with high photoresponsivity but lower mobility than that of graphene. Here, we propose a graphene/$MoSe_2$ barristor with a high-k ion-gel gate dielectric. It shows a high on/off ratio (3.3×10^4) and ambipolar behavior that is controlled by an external bias. The barristor exhibits very high external quantum efficiency (EQE, 66.3%) and photoresponsivity (285.0 mA/W). We demonstrate that an electric field applied to the gate electrode substantially modulates the photocurrent of the barristor, resulting in a high gate tuning ratio (1.50 μA/V). Therefore, this barristor shows potential for use as an ambipolar transistor with a high on/off ratio and a gate-tunable photodetector with a high EQE and responsivity.

Introduction

Graphene, a two-dimensional (2D) carbon atomic crystal, has attracted substantial interest for electronic applications[1] owing to its high intrinsic carrier mobility[2], excellent mechanical flexibility[3], optical transparency[4], and unique ambipolar transport characteristics[5]. In particular, its ambipolarity suggests that carriers can be tuned continuously between electrons and holes by supplying the required gate biases, enabling a wide variety of applications, including memory[6], frequency multipliers[7], high-frequency oscillators up to the THz range[8], and fast switches[9]. However, graphene-based transistors have not yet been implemented in real applications because of their low on/off ratio, which arises from graphene's gapless band structure[10]. A high on/off ratio has been obtained by introducing a barristor, that is, a gated graphene/Si junction, because the high junction resistance can provide a sufficiently low off-state current[11]. However, these barristors usually do not have the typical advantages of graphene, such as mechanical flexibility, optical transparency, and ambipolar transport properties, because Si and a low-k dielectric are used. Recently reported barristor structures, such as graphene/MoS_2 and graphene/WS_2, have shown very low mobility (40–60 $cm^2/V\,s$) compared to that of graphene[12].

Graphene photodetectors are being developed[13]. The high mobility of graphene enables high-speed extraction of the photogenerated carriers. However, graphene photodetectors, which typically use the local potential gradient near the graphene–metal junctions, have shown low external quantum efficiency (EQE) and responsivity owing to poor absorption and low built-in potential[14]. To overcome this problem, graphene photodetectors require extensive junctions rather than local junctions, as well as high mobility and a high built-in potential. Unlike graphene-based lateral photodetectors, which have a rather small photosensing active area near the

Correspondence: Bae Ho Park (baehpark@konkuk.ac.kr)
[1]Division of Quantum Phases & Devices, Department of Physics, Konkuk University, 120 Neungdong-ro, Gwangjin-gu, Seoul 05029, Republic of Korea
[2]Department of Physics and Department of Energy Systems Research, Ajou University, 206 World cup-ro, Yeongtong-gu, Suwon-si, Gyeonggi-do 16499, Republic of Korea

graphene–metal contact, the vertical barristor device generates a broad region of photocurrent throughout the vertical stack area[15–17]. In addition, barristor devices based on bonding with a high-absorption material may exhibit high absorption resulting from the high built-in potential. However, the 2D barristor devices have revealed limited optoelectronic performances due to their low carrier mobilities and poor gate tuning ratios[12,14].

Here, we propose a field-effect device with a graphene/$MoSe_2$ channel layer and a high-*k* ion-gel gate dielectric. The device shows a high on/off ratio (3.3×10^4) and ambipolar behavior that is controlled by an applied gate voltage. Modulation of the Fermi level (E_F) of graphene by applying a gate voltage (V_{SG}) is confirmed by the change in the Schottky barrier (SB) height (Φ_B) at the graphene/$MoSe_2$ junction. These field effects, including ambipolar behavior, are locally investigated using scanning photocurrent microscopy (SPCM). It is further demonstrated that an external electric field can be used to modulate the amplitude or even completely reverse the polarity of the photocurrent in the vertical junction of the graphene/$MoSe_2$ barristor device. The strong gating effect of the device results in a higher EQE (66.3%), responsivity (285.0 mA/W), and gate tuning ratio (1.50 μA/V) compared to those of pristine devices. Therefore, our graphene/$MoSe_2$ barristor with an ion-gel gate dielectric is a suitable candidate for use in ambipolar transistors with a high on/off ratio and gate-tunable broad-area photodetectors with a high EQE and responsivity.

Materials and methods

Single-layer graphene and few-layer $MoSe_2$ were fabricated by mechanical exfoliation on a SiO_2 (300 nm)/Si substrate. The SiO_2/Si substrate was cleaned with hot piranha solution ($H_2SO_4/H_2O_2 = 4{:}1$) to remove organic matter from its surface[18]. The electrodes were fabricated using electron beam lithography (Tescan Mira 2 and Raith Elphy Quantum Plus) and electron beam evaporation (Daeki-Hi-tech DKEB-02-04). Poly(methyl methacrylate) (PMMA) C4 solution was spin-coated on the layers at 4500 rpm, followed by baking at 180 °C for 2 min. Electron beam lithography at a dose of ~280 μC/cm^2 was used to define patterns on the spin-coated PMMA layer. Then, the Au (50 nm) source, drain, and gate electrodes were deposited on the graphene, $MoSe_2$, and SiO_2/Si substrate, respectively, by electron beam evaporation at a deposition rate of 0.4 Å/s and a pressure of 10^{-6} Torr. Graphene with two source electrodes was transferred to the sample on which $MoSe_2$, two drain electrodes, and one gate electrode were deposited. The graphene/$MoSe_2$ junction was formed between the source and drain electrodes. A polydimethylsiloxane well was located between the side gate and the graphene/$MoSe_2$ channel and filled with an ion-gel dielectric for the SPCM measurements[19,20].

Electrodes and markers were patterned on exfoliated graphene and $MoSe_2$ layers over SiO_2/Si substrates using electron beam lithography and electron beam evaporation systems. An ion gel was fabricated by gelation of a triblock copolymer in an ionic liquid[21]. An ultraviolet (UV) cross-linkable polyelectrolyte ion-gel dielectric layer was deposited on the graphene/$MoSe_2$ heterostructure as a gate dielectric. The ionic liquid 1-ethyl-3-methylimidazolium bis (trifluoromethylsulfonyl)imide, the monomer poly(ethyleneglycol) diacrylate (Mw = 575 g/mol), and the UV cross-linking initiator 2-hydroxy-2-methylpropiophenone were mixed at a weight-ratio of 88:8:4, and the mixed solution was dropped and spread on the graphene/$MoSe_2$ structure. The dropped solution was solidified by UV exposure (365 nm, 100 mW/cm^2) for 10 s. Finally, a side-gate graphene/$MoSe_2$ device with channel dimensions of 10 μm × 30 μm was obtained.

Results and discussion

Figure 1a shows a schematic diagram of the graphene/$MoSe_2$ barristor structure. High-quality single-layer graphene and few-layer $MoSe_2$ samples were prepared by mechanical exfoliation on a SiO_2 (300 nm thick)/Si substrate. The Au (50 nm) source, drain, and gate electrodes were deposited on the graphene, $MoSe_2$, and SiO_2/Si substrate, respectively, by electron beam evaporation. The device fabrication is described in detail in the "Materials and methods" section and Supplementary Information (Fig. S1).

Figure 1b shows an optical microscope image of a graphene/$MoSe_2$ barristor device. The blue and green areas surrounded by white dashed lines are graphene and $MoSe_2$, respectively. Two source and drain electrodes were used to check the electrical characteristics of graphene and $MoSe_2$, respectively. The electrical characteristics of the graphene/$MoSe_2$ barristor device were checked between one source and one drain electrode. The SPCM setup, which includes a transport measurement system, is illustrated in Fig. 1c and the Supplementary Information (Fig. S2). The graphene/$MoSe_2$ barristor device was illuminated by a diffraction-limited laser (spot diameter, ~500 nm; wavelength, 532 nm) while the device conductance was recorded as a function of the laser spot position. The small spot size (Supplementary Information, Fig. S3) enabled us to record the photoinduced electronic signal originating from light illumination on a specific part of the graphene/$MoSe_2$ barristor. Because the photocurrent is influenced by the potential profile, an SPCM image can provide information on the local potential profile. We simultaneously obtained a reflected light image to determine the position of the laser spot. Figure 1d shows a photocurrent image of the graphene/$MoSe_2$ barristor obtained at $V_{SG} = -1.0$ V. The yellow areas denote the source and drain electrodes. The color scale

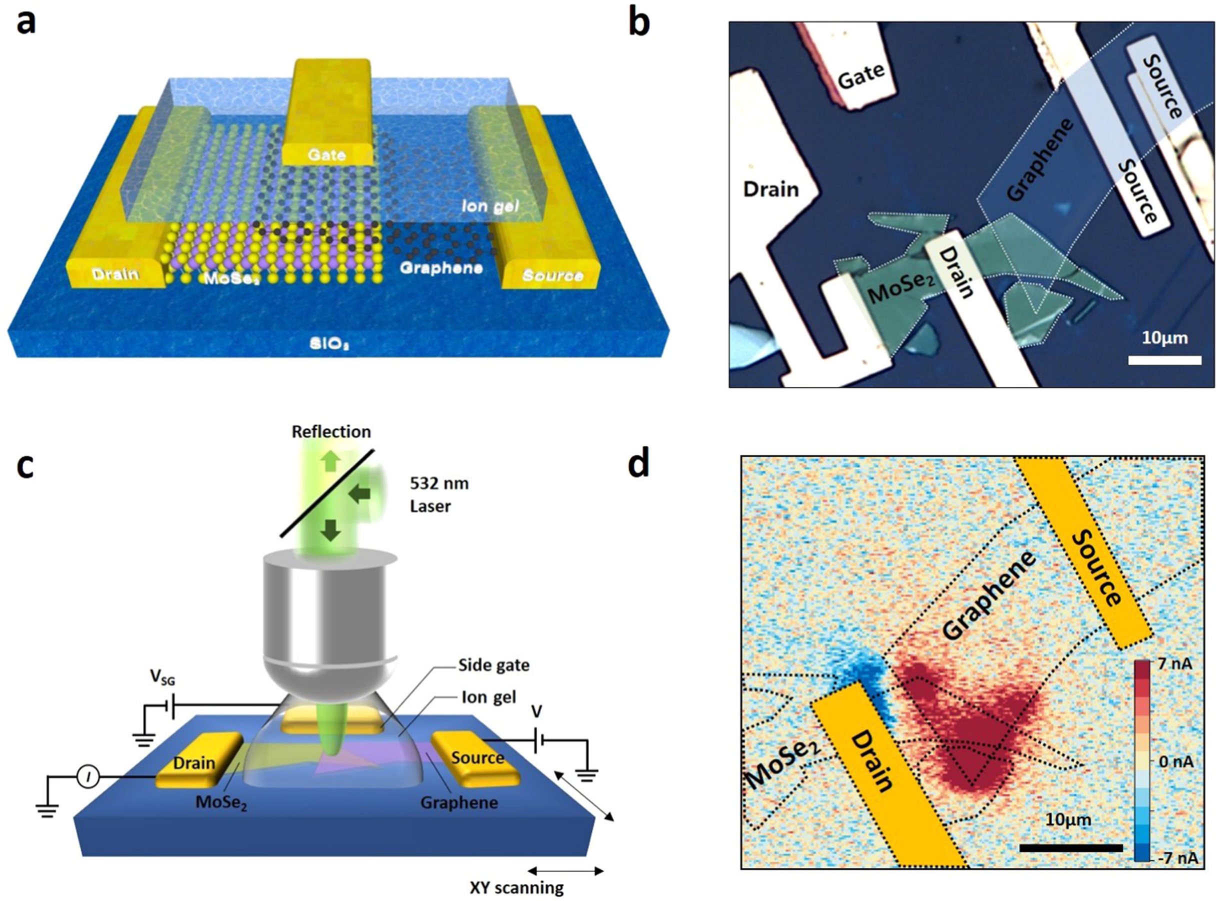

Fig. 1 Graphene/$MoSe_2$ barristor characterization. a Schematic diagram and **b** optical microscope image of the graphene/$MoSe_2$ barristor device. **c** Schematic of the SPCM measurement setup equipped with a transport measurement system. **d** SPCM image of the graphene/$MoSe_2$ barristor device obtained at $V_{SG} = -1.0$ V.

refers to the photocurrent measured between the source and drain electrodes at zero bias. The red area near the graphene/$MoSe_2$ junction corresponds to photocurrent flowing to the drain. The blue area near the $MoSe_2$/drain electrode junction corresponds to photocurrent flowing to the source. The generated photocurrent signals are attributed to band bending and the resultant local electric field at the graphene/$MoSe_2$ and $MoSe_2$/drain electrode junctions. The opposite photocurrent directions indicate the opposite directions of the local electric fields at the graphene/$MoSe_2$ and $MoSe_2$/drain electrode junctions.

Figure 2a shows the source–drain current amplitude ($|I_{SD}|$) vs. the source–drain voltage (V_{bias}) measured as V_{SG} increases from −1.25 to 0.5 V (right panel) and from 0.5 to 1.25 V (left panel) in 0.25 V steps. The orange and blue arrows indicate directions of changes in $|I_{SD}|$ with increasing V_{SG} in the *p*-type and *n*-type regions, respectively. The right panel shows typical *p*-type behavior, in which the current decreases as V_{SG} increases from −1.25 to 0.5 V. By contrast, the left panel shows typical *n*-type behavior, in which the current increases as V_{SG} increases from 0.5 to 1.25 V. We can confirm the ambipolar behavior (*p*-type and *n*-type characteristics) for $-1.25\ \mathrm{V} < V_{SG} < 1.25\ \mathrm{V}$. Note that we can control the type of graphene/$MoSe_2$ barristor device by changing the applied V_{SG}, as in an ambipolar graphene channel device.

Figure 2b shows the transfer characteristics of the graphene/$MoSe_2$ barristor device, which were measured as a function of V_{SG} at a fixed V_{bias} of 10 mV. These characteristics are different from those of graphene and $MoSe_2$ devices (Supplementary Information, Figs. S4 and S5, respectively). Our device shows a high on/off ratio of 3.3×10^4, which substantially exceeds those reported for pure graphene transistors (2–20). The barristor exhibits distinct ambipolar behavior and remarkably high carrier mobility values, specifically, an electron mobility of 247 cm^2/V s and a hole mobility of 182 cm^2/V s at room temperature. These values are determined using the following expression for the field-effect mobility: $\mu = (1/C_{SG}) \times (d\sigma/dV_{SG})$, where C_{SG} is the side-gate dielectric

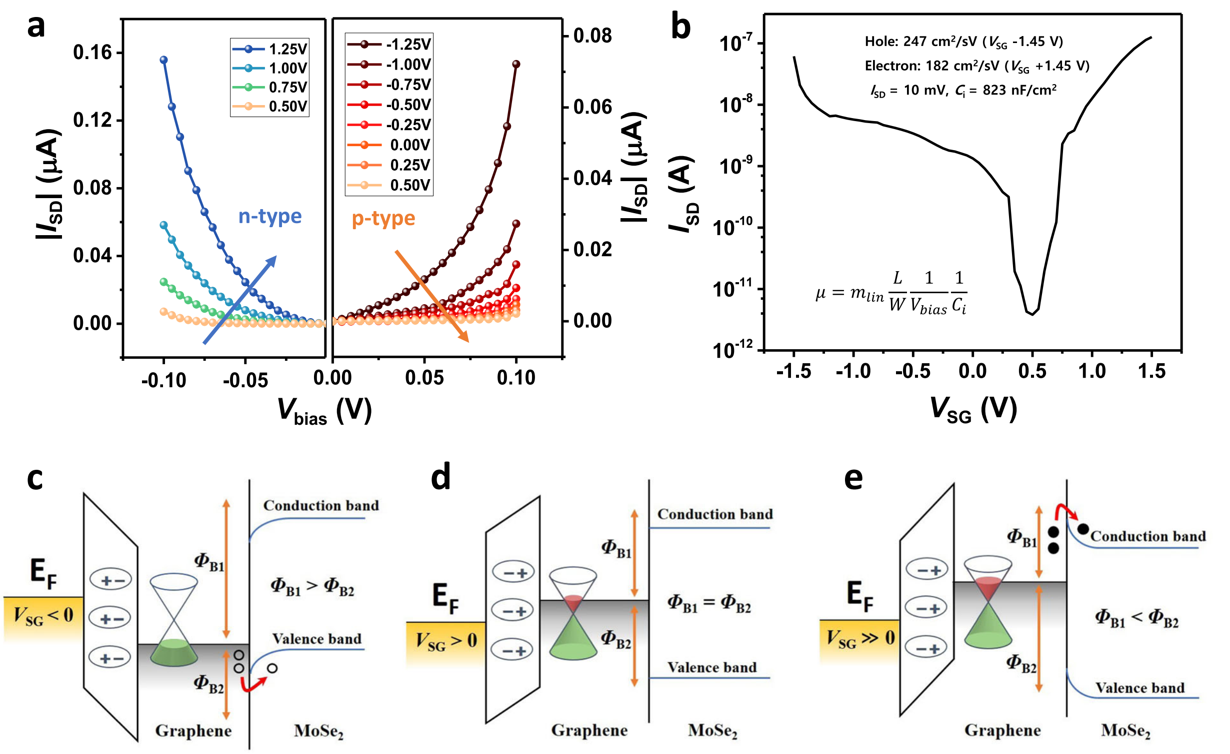

Fig. 2 Resistive switching behavior depending on the top electrode material. **a** $|I_{SD}|$–V_{bias} curves measured as V_{SG} increases from −1.25 to 0.5 V (right panel) and from 0.5 to −1.25 V (left panel) in 0.25 V steps. The orange and blue arrows indicate changes in the direction of $|I_{SD}|$ with increasing V_{SG} in *p*-type and *n*-type regions, respectively. **b** Transfer characteristics of the graphene/$MoSe_2$ barristor, which are measured as a function of V_{SG} at a fixed V_{bias} of 10 mV. Schematic band diagrams of the graphene/$MoSe_2$ barristor at **c** $V_{SG} < 0$, **d** $V_{SG} > 0$, and **e** $V_{SG} \gg 0$.

capacitance (Supplementary Information, Fig. S6). The conductivity is defined as $\sigma = I_{SD}/V_{bias} \times L/W$, where L is the length and W is the width of the barristor channel. Because this device does not have well-defined channel dimension, the mobility was calculated from the minimum value of L and the maximum value of W for identifying the lower bound of the mobility. The obtained mobility values have similar orders of magnitude to those reported for other barristor devices (40–60 $cm^2/V\,s$), such as graphene/MoS_2 and graphene/WS_2[12], and for $MoSe_2$ devices (50–160 $cm^2/V\,s$)[22–25].

The observed ambipolar behavior controlled by V_{SG} can be explained by using the schematic band diagrams of the graphene/$MoSe_2$ barristor at $V_{SG} < 0$ V, $V_{SG} > 0$ V, and $V_{SG} \gg 0$ V (Fig. 2c–e, respectively). Φ_{B1} and Φ_{B2} indicate the barrier heights for electrons and holes, respectively, at the graphene/$MoSe_2$ interface. Because of the observed *p*-type behavior at $V_{SG} < 0$ V, we can assume that $\Phi_{B1} > \Phi_{B2}$ at $V_{SG} < 0$ V (Fig. 2c). If the E_F of graphene is near the valence band of $MoSe_2$, holes become the majority carriers, so a *p*-type SB forms at the graphene/$MoSe_2$ junction[3]. As the gate voltage increases, Φ_{B2} also increases, and hole transport becomes more difficult. Conversely, as the gate voltage decreases, Φ_{B2} also decreases, and hole transport becomes easier. The E_F of graphene can be increased by the applied positive V_{SG} so that $\Phi_{B1} = \Phi_{B2}$ and even $\Phi_{B1} < \Phi_{B2}$, as shown in Fig. 2d, e, respectively. When $\Phi_{B1} < \Phi_{B2}$ at $V_{SG} \gg 0$ V, electrons become the majority carriers, and the graphene/$MoSe_2$ barristor exhibits *n*-type behavior, as shown in Fig. 2e. As the gate voltage increases, Φ_{B1} decreases, and electron transport becomes easier. Conversely, as the gate voltage decreases, Φ_{B1} increases, and electron transport becomes more difficult. The substantial change in the E_F of graphene is attributed to the small area of the Fermi surface and the introduction of the ion-gel gate dielectric. In addition, because $MoSe_2$ has a small band gap and similarly high-mobility values (50–160 $cm^2/V\,s$) for electrons and holes, the relative sizes of Φ_{B1} and Φ_{B2} can be controlled by modulating the E_F of graphene.

To investigate the local field effect, we performed SPCM measurements of the graphene/$MoSe_2$ barristor shown in Fig. 3a at various gate voltages. Figure 3b–d show photocurrent images of the barristor at various gate voltages between −1.0 and 1.0 V. Because of the side-gate structure and transparent ion-gel dielectric, the illumination light reaches the barristor device without substantial loss. The blue dashed line, red dashed line, and yellow areas

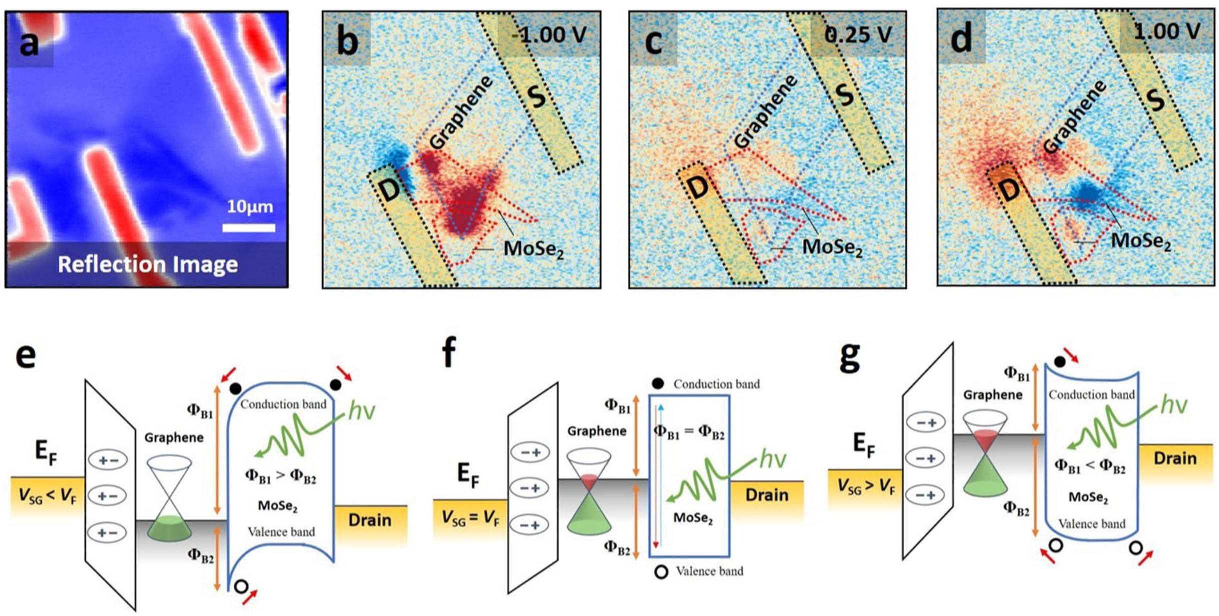

Fig. 3 Field-effect change in the local photocurrent of the graphene/$MoSe_2$ barristor device. **a** Reflection image and **b**–**d** SPCM images of the graphene/$MoSe_2$ barristor device obtained at V_{SG} values of −1.0 to 1.0 V. The blue dashed line, red dashed line, and yellow area denote graphene, $MoSe_2$, and the electrodes, respectively. Schematic band diagrams of the graphene/$MoSe_2$ device at **e** $V_{SG} < V_F$, **f** $V_{SG} = V_F$, and **g** $V_{SG} > V_F$, which correspond to $\Phi_{B1} > \Phi_{B2}$, $\Phi_{B1} = \Phi_{B2}$, and $\Phi_{B1} < \Phi_{B2}$.

denote graphene, $MoSe_2$, and the electrodes, respectively. Unlike a graphene-based lateral photodetector, which has a rather small photosensing active area near the graphene–metal contact, our vertical barristor device clearly shows a broad area of photocurrent generation throughout the junction of the vertical graphene/$MoSe_2$ stack. When a V_{SG} of −1.0 V is applied from the side gate (Fig. 3b), the SPCM images show a red area corresponding to photocurrent flowing to the drain electrode at the graphene/$MoSe_2$ junctions and a blue area corresponding to photocurrent flowing to the source electrode at the $MoSe_2$/drain electrode junction. Under a V_{SG} of 0.25 V (Fig. 3c), the photocurrent contrast signal at the graphene/$MoSe_2$ and $MoSe_2$/drain electrode junctions disappears. As V_{SG} increases to 1.0 V, the photocurrent contrast at the $MoSe_2$/drain electrode junction changes to red, whereas blue and red photocurrents are presented on the graphene/$MoSe_2$ heterojunction (Fig. 3d). It seems that the blue and red photocurrents on the graphene/$MoSe_2$ heterojunction may be caused by the spatial inhomogeneity of the graphene/$MoSe_2$ device. Because we used the side gate configuration and a liquid ion gel, the field effect on the graphene/$MoSe_2$ junction may depend on the location of the 2D planar device. The changes in photocurrent direction at both junctions demonstrate manipulation of the local potential profile and inversion of the band bending at each junction, which are obtained by varying V_{SG} in this vertically stacked device. Importantly, because of the finite density of states in graphene and the weak electrostatic screening effect, the graphene/$MoSe_2$ SB height can be effectively modulated by applying an external field through the side-gate electrode[26–28].

Figure 3e–g show schematic band diagrams of the graphene/$MoSe_2$ and $MoSe_2$/drain electrode junctions at various V_{SG} values. Modulation of the E_F of graphene and $MoSe_2$ can directly affect the band bending and photocurrent characteristics at the junctions. Because of the quantum capacitance and partial electrostatic transparency of graphene, the applied V_{SG} not only modulates the E_F of graphene but also penetrates graphene to accumulate/invert space charges within $MoSe_2$[29]. In graphene/$MoSe_2$ barristor devices, the change in E_F of graphene is very important. Therefore, we calculated ΔE_F using $\Delta E_F = \hbar v_F \sqrt{\pi n}$. Here, $\hbar$ is the Dirac constant, v_F is the Fermi velocity of graphene (1.0×10^6 m/s), and n is the carrier density[11,30]. The hole carrier density at $V_{SG} = -1.50$ V and electron carrier density at $V_{SG} = 1.45$ V of our graphene/$MoSe_2$ barristor device are determined to be 1.03×10^{13} and 4.88×10^{12} cm^{-2}, respectively. The calculated ΔE_F is −0.37 eV at $V_{SG} = -1.50$ V and 0.26 eV at $V_{SG} = 1.45$ V. The amount of change in E_F of 0.63 eV at the graphene/$MoSe_2$ barristor device obtained when V_{SG} varies between −1.50 and 1.45 V is larger than that of other barristor devices[11,30]. We define V_F as the applied V_{SG} at which $\Phi_{B1} = \Phi_{B2}$, which results in a flat band in

$MoSe_2$. When the E_F value of graphene is reduced at $V_{SG} < V_F$, holes become the majority carriers, resulting in a *p*-type SB with downward band bending at the graphene/$MoSe_2$ junction. Then, the photoexcited electrons near the graphene/$MoSe_2$ junction drift toward the graphene to produce a positive photocurrent to the drain electrode (Fig. 3e). Similarly, *p*-type band bending causes photoexcited electrons near the $MoSe_2$/drain electrode to drift toward the drain electrode, resulting in a negative photocurrent to the source electrode. When the E_F values of graphene and $MoSe_2$ are increased at $V_{SG} = V_F$, the band bending of $MoSe_2$ at the interfaces becomes negligible, resulting in easy recombination of photoexcited electrons and holes before the photocurrent forms (Fig. 3f). When the E_F value of graphene is higher at $V_{SG} > V_F$, electrons become the majority carriers, resulting in an *n*-type SB with upward band bending at the graphene/$MoSe_2$ junction. Then, the photoexcited holes near the graphene/$MoSe_2$ junction drift toward the graphene to produce a negative photocurrent to the source electrode (Fig. 3g). Similarly, *n*-type band bending causes the photoexcited holes near the $MoSe_2$/drain electrode to drift toward the drain electrode, resulting in a positive photocurrent to the drain electrode. Various graphene/$MoSe_2$ devices showed similar photocurrent images obtained at $V_{SG} = 0\,V$ (Supplementary Information, Fig. S7).

Figure 4a shows the gate dependence of the local photocurrent measured along the black line in the inset SPCM image in Fig. 4a as V_{SG} is swept from −1.0 to 1.0 V in 0.01 V steps. We measured the photocurrent by applying very low laser power (0.407 $\mu W/cm^2$) without a bias voltage. At $V_{SG} < V_F$, positive (red contrast) and negative (blue contrast) photocurrents are generated at the graphene/$MoSe_2$ (1) and $MoSe_2$/drain electrode (2) junctions, respectively. This photocurrent polarity is a result of *p*-type band bending, in which the E_F of graphene becomes closer to the valence band of $MoSe_2$, as shown in the band diagram in Fig. 3e. This result implies that the photogenerated electrons at the $MoSe_2$/drain electrode and graphene/$MoSe_2$ junctions are collected by the drain and source electrodes, respectively, as reported in previous studies of semiconducting devices with *p*-type bending[31–33]. At each junction point, the photocurrent polarity is inverted at $V_{SG} \sim 0.25\,V$. In addition, the polarity changes continuously from positive to negative (negative to positive) near the graphene/$MoSe_2$ junction ($MoSe_2$/drain electrode) as V_{SG} is swept from −1.0 to 1.0 V. At $V_{SG} > V_F$, negative and positive photocurrents are generated at the graphene/$MoSe_2$ (1) and $MoSe_2$/drain electrode (2) junctions, respectively. This photocurrent polarity can be interpreted as *n*-type band bending, in which the E_F of graphene becomes closer to the conduction band of $MoSe_2$, as shown in the band diagram in Fig. 3g. This result implies that the photogenerated holes at the $MoSe_2$/drain electrode and graphene/$MoSe_2$ junctions are collected by the drain and source electrodes, respectively, as reported in previous studies of semiconducting devices with *n*-type bending[34]. The graphene/$MoSe_2$ barristor device shows ambipolar behavior with *p*-type and *n*-type characteristics at $V_{SG} < V_F$ and $V_{SG} > V_F$, respectively. Because the intensity of the photocurrent was roughly proportional to the local electric field or the slope of the electrostatic potential, we qualitatively examined the electrostatic potential along the device by integrating the photocurrent line profile at V_{SG} values ranging from −1.0 to 1.0 V in 0.25 V steps.

Figure 4b presents the resulting electrostatic potential profile measured along the black line in the inset SPCM image in Fig. 4a. The measured photocurrent signal $[I_{ph}(x)]$ (Fig. 4b, inset) is proportional to the potential gradient as follows[34]:

$$I_{ph}(x) \propto -\frac{d\phi(x)}{dx}$$

where x denotes the position along the device channel, and $\phi(x)$ is the electrostatic potential. The potential changes dramatically near the graphene/$MoSe_2$ (1) and $MoSe_2$/drain electrode (2) contact regions, indicating SB formation at the graphene/$MoSe_2$ junction (1) and $MoSe_2$/drain electrode (2). Note that the change in potential at the graphene/$MoSe_2$ junction with changing V_{SG} is 13-fold larger than that at the $MoSe_2$/drain electrode. This finding implies that the graphene/$MoSe_2$ junction can become a potential element for tunable electronic or optoelectronic devices.

Figure 4c, d show photocurrent vs. V_{SG} data obtained at the graphene/$MoSe_2$ and $MoSe_2$/drain electrode junctions, respectively. At the graphene/$MoSe_2$ junction, the positive photocurrent decreases as V_{SG} increases from −1.0 to 0.4 V, and the photocurrent becomes negative at $V_{SG} = 0.4\,V$. When V_{SG} is −0.98 V, we obtain a very high gate tuning ratio of ~76.6 nA/V, which is defined as the ratio of the change in photocurrent amplitude to the change in V_{SG}. At the $MoSe_2$/drain electrode junction, negative and positive photocurrents are generated at $-1.0\,V < V_{SG} < 0.15\,V$ and $0.15\,V < V_{SG} < 1.0\,V$, respectively. When V_{SG} is −0.71 V, we obtain a high gate tuning ratio of ~18.2 nA/V. We could obtain a higher gate tuning ratio of 1.50 μA/V at a graphene/$MoSe_2$ junction in another barristor device (Supplementary Information, Fig. S8). These gate tuning ratios, which were measured at a very low laser power (0.407 $\mu W/cm^2$), are much higher than those of other graphene-based devices (1–5 nA/V)[35]. In addition, the very high gating effect of our graphene/$MoSe_2$ barristor structure with a high-k ion-gel gate dielectric dramatically changes the polarity of the photocurrent. The high gate-tunability of the photocurrent is significant for the facile modulation of sensitivity for optical sensors. In dark spaces (such as a tunnel and cinema) where the physical

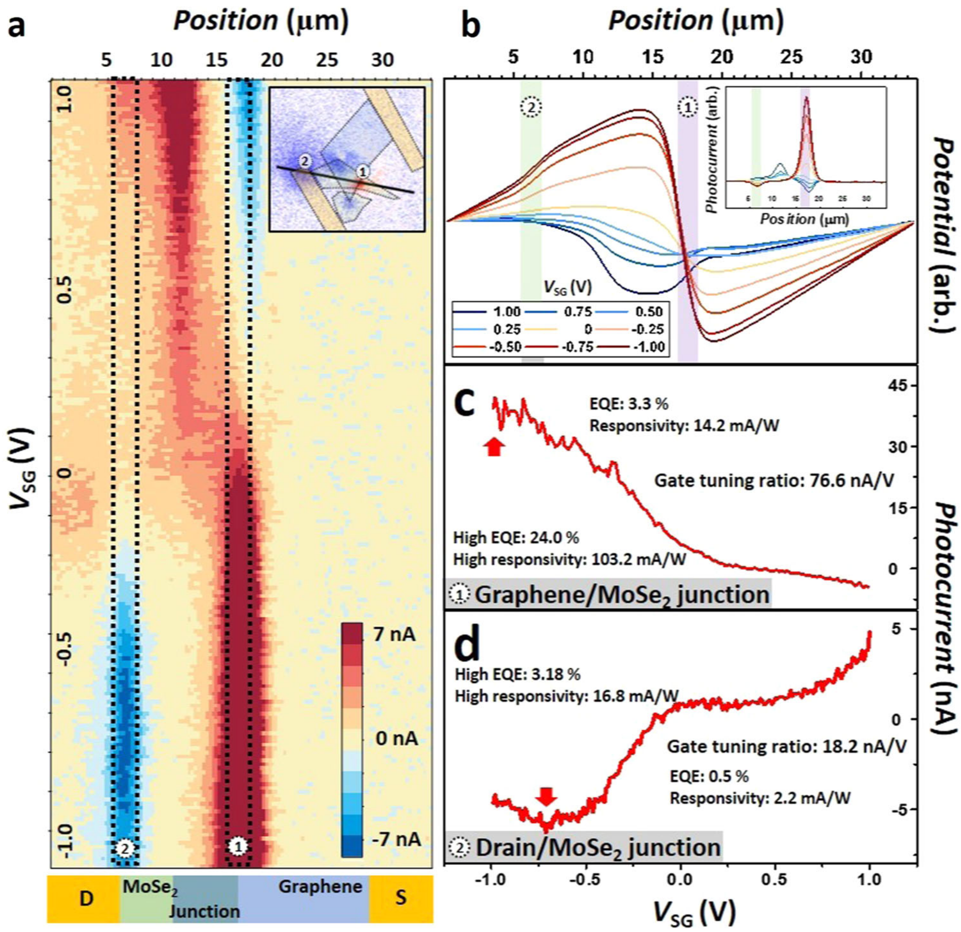

Fig. 4 Field-effect modulation of photocurrent at junctions in graphene/$MoSe_2$. a Gate voltage dependence of photocurrent measured along the black line of the SPCM image (inset). **b** Electrostatic potential profile obtained by numerical integration of the experimental accumulated photocurrent amplitudes. The inset shows the photocurrent along the graphene/$MoSe_2$ barristor device at V_{SG} values ranging from −1.0 to 1.0 V in 0.25 V steps. Photocurrent vs. V_{SG} data obtained at the **c** graphene/$MoSe_2$ and **d** $MoSe_2$/drain electrode junctions.

environment is limited, photosensitivity should be amplified so that sufficient photocurrent can be secured. In bright spaces (such as outdoors on a sunny day), photosensitivity can be reduced and the value of photocurrent flowing through the device can be constantly adjusted. Therefore, the development of high-gate tuning elements in optical devices is very necessary[35,36].

Using the photocurrent response and input laser power, we can determine the EQE and photoresponsivity. The photoresponsivity (R_I) is defined as the ratio of the electrical current response to the incident optical power ($R_I = I_{ph}/P_{opt}$)[16,37]. The EQE (η) is defined as the number of carriers produced per photon and is expressed as

$$\eta = \frac{I_{ph}}{q\Phi} = \frac{I_{ph}}{q}\left(\frac{h\nu}{P_{opt}}\right)$$

where I_{ph} is the photocurrent, Φ is the photon flux ($=P_{opt}/h\nu$), h is the Planck constant, ν is the frequency of the light, q is the electron charge, and P_{opt} is the optical power. At the graphene/$MoSe_2$ junction, the EQE increases from 3.3% (corresponding to a photoresponsivity of 14.2 mA/W) at $V_{SG} = 0$ V to 24.0% (corresponding to a photoresponsivity of 103.2 mA/W) at $V_{SG} = -0.98$ V under excitation at a laser power of 0.407 µW/cm^2. At the $MoSe_2$/drain electrode junction, the EQE increased from 0.5% (corresponding to a photoresponsivity of 2.2 mA/W) at $V_{SG} = 0$ V to 3.18% (corresponding to a photoresponsivity of 16.8 mA/W) at $V_{SG} = -0.71$ V. The EQE at the graphene/$MoSe_2$ junction is ~6.6-fold larger than that at the $MoSe_2$/drain electrode junction at $V_{SG} = 0$ V. The EQE (24%) observed at the vertical graphene/$MoSe_2$ junction at $V_{SG} = -0.98$ V is two orders of magnitude higher than those of lateral metal–graphene–metal photodetectors (EQE ≈ 0.1–0.2%)[14,38,39]. We could obtain a higher EQE of 66.3% and photoresponsivity of 285.0 mA/W at a graphene/$MoSe_2$ junction in another barristor device (Supplementary Information, Fig. S8). This high EQE is due primarily to more efficient photon absorption in the broad area of the vertical barristor device and more efficient charge separation resulting from a much larger band offset and a much higher mobility[16].

Conclusion

In summary, we fabricated a graphene/$MoSe_2$ barristor with a high-k ion-gel gate dielectric. The graphene/$MoSe_2$ device showed a high on/off ratio (3.3×10^4) and ambipolar behavior that was controlled by an applied gate voltage. SPCM measurements revealed that the graphene/$MoSe_2$ barristor had very high EQE (66.3%) and photoresponsivity (285.0 mA/W) values, making it suitable for highly efficient photocurrent generation and photodetection. We further demonstrated that an electric field applied to the gate electrode could substantially modulate the amplitude and polarity of the photocurrent at the graphene/$MoSe_2$ junction, resulting in a high gate tuning ratio (1.50 μA/V). Therefore, the graphene/$MoSe_2$ barristor with a high-k ion-gel gate dielectric is a suitable candidate for use in ambipolar transistors (with a high on/off ratio) and gate-tunable photodetectors (with a high EQE and responsivity).

Acknowledgements

This work was supported by National Research Foundation of Korea (NRF) grants funded by the Korean government (MSIP) (No. 2013R1A3A2042120) and the KIST Institutional Program (No. 2E30410-20-085).

Author contributions

G.O. and B.H.P. planned the projects and designed the experiments. G.O. fabricated and characterized graphene/$MoSe_2$ barristors. Y.C.K., Y.H.A. and G.O. performed the SPCM experiment. G.O., J.J., and B.H.P. interpreted the results. All the authors participated in discussions and writing the manuscript.

Conflict of interest

The authors declare that they have no conflict of interest.

Supplementary information Supplementary information is available for this paper at https://doi.org/10.1038/s41427-021-00281-4.

Received: 28 July 2020 Revised: 20 November 2020 Accepted: 2 December 2020.
Published online: 29 January 2021

References

1. Novoselov, K. S. et al. A roadmap for graphene. *Nature* **490**, 192–200 (2012).
2. Mayorov, A. S. et al. Micrometer-scale ballistic transport in encapsulated graphene at room temperature. *Nano Lett.* **11**, 2396–2399 (2011).
3. Bae, S. et al. Roll-to-roll production of 30-inch graphene films for transparent electrodes. *Nat. Nanotechnol.* **5**, 574–578 (2010).
4. Nair, R. R. et al. Fine structure constant defines visual transparency of graphene. *Science* **320**, 1308 (2008).
5. Geim, A. K. & Novoselov, K. S. The rise of graphene. *Nat. Mater.* **6**, 183–191 (2007).
6. Myung, S., Park, J., Lee, H., Kim, K. S. & Hong, S. Ambipolar memory devices based on reduced graphene oxide and nanoparticles. *Adv. Mater.* **22**, 2045–2049 (2010).
7. Wang, Z. et al. Large signal operation of small band-gap carbon nanotube-based ambipolar transistor: a high-performance frequency doubler. *Nano Lett.* **10**, 3648–3655 (2010).
8. Vicarelli, L. et al. Graphene field-effect transistors as room-temperature terahertz detectors. *Nat. Mater.* **11**, 865–871 (2012).
9. Newns, D. M., Elmegreen, B. G., Liu, X. H. & Martyna, G. J. High response piezoelectric and piezoresistive materials for fast, low voltage switching: simulation and theory of transduction physics at the nanometer-scale. *Adv. Mater.* **24**, 3672–3677 (2012).
10. Kim, B. J. et al. High-performance flexible graphene field effect transistors with ion gel gate dielectrics. *Nano Lett.* **10**, 3464–3466 (2010).
11. Yang, H. et al. Graphene barristor, a triode device with a gate-controlled Schottky barrier. *Science* **336**, 1140–1143 (2012).
12. Solís-Fernández, P., Bissett, M. & Ago, H. Synthesis, structure and applications of graphene-based 2D heterostructures. *Chem. Soc. Rev.* **46**, 4572–4613 (2017).
13. Xia, F., Mueller, T., Lin, Y., Valdes-Garcia, A. & Avouris, P. Ultrafast graphene photodetector. *Nat. Nanotechnol.* **4**, 839–843 (2009).
14. Liu, Y. et al. Plasmon resonance enhanced multicolour photodetection by graphene. *Nat. Commun.* **2**, 579 (2011).
15. Yu, W. J. et al. Highly efficient gate-tunable photocurrent generation in vertical heterostructures of layered materials. *Nat. Nanotechnol.* **8**, 952–958 (2013).
16. Liu, N. et al. Large-area, transparent, and flexible infrared photodetector fabricated using PN junctions formed by N-doping chemical vapor deposition grown graphene. *Nano Lett.* **14**, 3702–3708 (2014).
17. De Fazio, D. et al. High responsivity, large-area graphene/MoS2 flexible photodetectors. *ACS Nano* **10**, 8252–8262 (2016).
18. Zhao, S. & Liu, H. Bottom-up nanofabrication through catalyzed vapor phase HF etching of SiO2. *Nanotechnology* **26**, 015301 (2014).
19. Kim, Y. C., Nguyen, V. T., Lee, S., Park, J. Y. & Ahn, Y. H. Evaluation of transport parameters in MoS2/graphene junction devices fabricated by chemical vapor deposition. *ACS Appl. Mater. Interfaces* **10**, 5771–5778 (2018).
20. Yoon, J. H. et al. Electronic band alignment at complex oxide interfaces measured by scanning photocurrent microscopy. *Sci. Rep.* **7**, 3824 (2017).
21. Oh, G. et al. Graphene/pentacene barristor with ion-gel gate dielectric: flexible ambipolar transistor with high mobility and on/off ratio. *ACS Nano* **9**, 7515–7522 (2015).
22. Abderrahmane, A. et al. High photosensitivity few-layered MoSe2 back-gated field-effect phototransistors. *Nanotechnology* **25**, 365202 (2014).
23. Wang, X. et al. Chemical vapor deposition growth of crystalline monolayer MoSe2. *ACS Nano* **8**, 5125–5131 (2014).
24. Rhyee, J. S. et al. High-mobility transistors based on large-area and highly crystalline CVD-grown MoSe2 films on insulating substrates. *Adv. Mater.* **28**, 2316–2321 (2016).
25. Chamlagain, B. et al. Mobility improvement and temperature dependence in MoSe2 field-effect transistors on parylene-C substrate. *ACS Nano* **8**, 5079–5088 (2014).
26. Britnell, L. et al. Field-effect tunneling transistor based on vertical graphene heterostructures. *Science* **335**, 947–950 (2012).
27. Yu, W. J. et al. Vertically stacked multi-heterostructures of layered materials for logic transistors and complementary inverters. *Nat. Mater.* **12**, 246–252 (2013).
28. Georgiou, T. et al. Vertical field-effect transistor based on graphene–WS2 heterostructures for flexible and transparent electronics. *Nat. Nanotechnol.* **8**, 100–103 (2013).
29. Liu, Y. et al. Ambipolar barristors for reconfigurable logic circuits. *Nano Lett.* **17**, 1448–1454 (2017).
30. Shim, J. & Park, J. Optimization of graphene–MoS2 barristor by 3-aminopropyltriethoxysilane (APTES). *Org. Electron.* **33**, 172–177 (2016).
31. Ahn, Y., Dunning, J. & Park, J. Scanning photocurrent imaging and electronic band studies in silicon nanowire field effect transistors. *Nano Lett.* **5**, 1367–1370 (2005).

32. Ahn, Y. H., Tsen, A. W., Kim, B., Park, Y. W. & Park, J. Photocurrent imaging of *p*—*n* junctions in ambipolar carbon nanotube transistors. *Nano Lett*. **7**, 3320–3323 (2007).
33. Park, J. K., Son, B. H., Park, J. Y., Lee, S. & Ahn, Y. H. High-speed scanning photocurrent imaging techniques on nanoscale devices. *Curr. Appl. Phys*. **13**, 2076–2081 (2013).
34. Engel, M. et al. Spatially resolved electrostatic potential and photocurrent generation in carbon nanotube array devices. *ACS Nano* **6**, 7303–7310 (2012).
35. Zhang, Y. et al. Broadband high photoresponse from pure monolayer graphene photodetector. *Nat. Commun*. **4**, 1811 (2013).
36. Youngblood, N., Anugrah, Y., Ma, R., Koester, S. J. & Li, M. Multifunctional graphene optical modulator and photodetector integrated on silicon waveguides. *Nano Lett*. **14**, 2741–2746 (2014).
37. An, X., Liu, F., Jung, Y. J. & Kar, S. Tunable graphene–silicon heterojunctions for ultrasensitive photodetection. *Nano Lett*. **13**, 909–916 (2013).
38. Echtermeyer, T. J. et al. Strong plasmonic enhancement of photovoltage in graphene. *Nat. Commun*. **2**, 458 (2011).
39. Xia, F. et al. Photocurrent imaging and efficient photon detection in a graphene transistor. *Nano Lett*. **9**, 1039–1044 (2009).